Numerical analysis of unsteady cavitating turbulent flow and shedding horse-shoe vortex structure around a twisted hydrofoil

Bin Ji [a], Xianwu Luo [a,*], Yulin Wu [a], Xiaoxing Peng [b], Yunling Duan [a]

[a] State Key Laboratory of Hydroscience & Engineering, Tsinghua University, Beijing 100084, China
[b] China Ship Scientific Research Center, Wuxi 214082, China

ABSTRACT

Cavitating turbulent flow around hydrofoils was simulated using the Partially-Averaged Navier–Stokes (PANS) method and a mass transfer cavitation model with the maximum density ratio ($\rho_l/\rho_{v,\mathrm{clip}}$) effect between the liquid and the vapor. The predicted cavity length and thickness of stable cavities as well as the pressure distribution along the suction surface of a NACA66(MOD) hydrofoil compare well with experimental data when using the actual maximum density ratio ($\rho_l/\rho_{v,\mathrm{clip}} = 43391$) at room temperature. The unsteady cavitation patterns and their evolution around a Delft twisted hydrofoil were then simulated. The numerical results indicate that the cavity volume fluctuates dramatically as the cavitating flow develops with cavity growth, destabilization, and collapse. The predicted three dimensional cavity structures due to the variation of attack angle in the span-wise direction and the shedding cycle as well as its frequency agree fairly well with experimental observations. The distinct side-lobes of the attached cavity and the shedding U-shaped horse-shoe vortex are well captured. Furthermore, it is shown that the shedding horse-shoe vortex includes a primary U-shaped vapor cloud and two secondary U-shaped vapor clouds originating from the primary shedding at the cavity center and the secondary shedding at both cavity sides. The primary shedding is related to the collision of a radially-diverging re-entrant jet and the attached cavity surface, while the secondary shedding is due to the collision of side-entrant jets and the radially-diverging re-entrant jet. The local flow fields show that the interaction between the circulating flow and the shedding vapor cloud may be the main mechanism producing the cavitating horse-shoe vortex. Two side views described by iso-surfaces of the vapor volume fraction for a 10% vapor volume, and a non-dimensional Q-criterion equal to 200 are used to illustrate the formation, roll-up and transport of the shedding horse-shoe vortex. The predicted height of the shedding horse-shoe vortex increases as the vortex moves downstream. It is shown that the shape of the horse-shoe vortex for the non-dimensional Q-criterion is more complicated than that of the 10% vapor fraction iso-surface and is more consistent with the experiments. Further, though the time-averaged lift coefficient predicted by the PANS calculation is about 12% lower than the experimental value, it is better than other predictions based on RANS solvers.

© 2012 Elsevier Ltd. Open access under CC BY-NC-ND license.

1. Introduction

The unsteady behavior of cavitating flows and cavity shedding still attract much attention since they seriously affect the hydrodynamic performance of blades and propellers. Cavitation control is expected to improve the performance and reliability of hydraulic machines (Arndt, 1981).

In the past decades, much research, including experiments and simulations, have been conducted to understand the mechanisms of unsteady cavity shedding with unsteady cavitation studied extensively for two-dimensional cases (Coutier-Delgosha et al., 2003; Goncalves, 2011; Gopalan and Katz, 2000; Huang and Wang, 2011; Kawanami et al., 1997; Kjeldsen et al., 2000; Kunz et al., 2000; Laberteaux and Ceccio, 2001a; Le et al., 1993; Pham et al., 1999; Senocak and Shyy, 2004b; Stutz and Reboud, 1997). Though they are valuable as basic studies, blades and propellers on hydraulic machines have not only three-dimensional geometries but also non-uniform loading in the span-wise direction. Thus, the cavitation topology and the three-dimensional effects on cavitation should be investigated. De Lange and De Bruin (1998) tested transparent hydrofoils in a cavitation tunnel to show that the re-entrant jet velocity component normal to the cavity closure line was reflected into the cavity in the three-dimensional case, though the jet for the two-dimensional hydrofoil was directed upstream. Laberteaux and Ceccio (2001b) showed for a series of swept

* Corresponding author. Tel./fax: +86 10 62789853.
  E-mail addresses: jibin@mail.tsinghua.edu.cn (B. Ji), luoxw@mail.tsinghua.edu.cn (X. Luo).

wedges that the cavity instability was greatly influenced by the span-wise pressure gradients and the re-entrant jet may be directed away from the cavity interface, allowing sheet cavitation to form a cloud cavitation far downstream. Dular et al. (2007) numerically and experimentally investigated re-entrant jet reflection at an inclined cavity closure line around a hydrofoil with an asymmetric leading edge. Dang and Kuiper (1999) numerically studied a re-entrant jet using a hydrofoil with various angles of attack in the spanwise direction. They found that the direction of the re-entrant jet was strongly influenced by the cavity topology and the change in the cavity shape was determined not by the sweep angle but by the loading. Saito et al. (2007) investigated cavitating flows around a three-dimensional hydrofoil with uniform profiles and uniform attack angles along the spanwise direction and pointed out that the sidewall effect is the main reason for generation of the U-shaped cavitation. Kawanami et al. (2002) experimentally demonstrated that cloud cavitation consisted of one vortex cavity with many cavity bubbles surrounding the main vortex which might be a U-shaped structure as a whole (one head and two legs). Schnerr et al. (2008) modeled the three-dimensional cloud cavitation around a 3D twisted hydrofoil and analyzed the 3D shock dynamics produced by the collapsing vapor cloud, which was consistent with experimental tests (Reisman et al., 1998). Koop and Hoeijmakers (2009) used a compressible unsteady Euler solver to predict the structure and dynamics of three sheet cavities and analyzed the collapse of the shedding vapor structure as well as the resulting high pressure. Recently, the cavitating flows around the Delft twisted hydrofoil, which was studied experimentally by Foeth et al. (Foeth, 2008; Foeth et al., 2006; Foeth et al., 2008), were utilized as benchmark data in two workshops, VIRTURE WP4 (Salvatore et al., 2009) and SMP11 (Hoekstra et al., 2011), because it resembles propeller cavitation well defined and easily studied. They clarified that the shedding of the sheet cavity was governed by the direction and momentum of the re-entrant and side-entrant jets and their impingement on the free surface of the cavity.

This paper presents unsteady numerical simulations of cavitating turbulent flow around the 3D twisted Delft hydrofoil to predict the 3D shedding cavity structure, including the cavitation development, cavity shedding and collapse. The calculations involve a mass transfer cavitation model based on the maximum density ratio effect with the PANS method for the turbulent modeling to secure better accuracy. Calculations were conducted to analyze the three-dimensional shedding cavity structure of cavitation. The unsteady cavitation behavior and the evolution of the horse-shoe vortex cavity are analyzed based on the calculations and experimental results.

2. PANS methodology and cavitation model

The PANS model is a bridging method from the RANS to DNS, which was first proposed by Girimaji (2006). This model can remarkably improve the accuracy of numerical results and has been proved by several publications in non-cavitating case (Jeong and Girimaji, 2010; Lakshmipathy and Girimaji, 2007, 2010; Ma et al., 2011; Song and Park, 2009). In present paper, PANS model is used together with a mixture model to simulate unsteady cavitating flow around a Delft twisted hydrofoil.

In present simulations, the commercial CFD code ANSYS-CFX is used to implement PANS model. The choice of ANSYS-CFX as the computational platform is due to the reason that it is one of the most widely used commercial code for engineering applications. It is important that the capabilities of PANS are demonstrated on ANSYS-CFX rather than on an in-house code.

In ANSYS-CFX, the vapor/liquid two-phase mixture model assumes that the fluid is homogeneous, so the multiphase fluid components share the same velocity and pressure. The continuity and momentum equations for the mixture flow are:

$$\frac{\partial \rho}{\partial t} + \frac{\partial (\rho u_j)}{\partial x_j} = 0 \tag{1}$$

$$\frac{\partial (\rho u_i)}{\partial t} + \frac{\partial (\rho u_i u_j)}{\partial x_j} = \rho f_i - \frac{\partial p}{\partial x_j} + \frac{\partial}{\partial x_j}\left[(\mu + \mu_t)\left(\frac{\partial u_i}{\partial x_j} + \frac{\partial u_j}{\partial x_i} - \frac{2}{3}\frac{\partial u_k}{\partial x_k}\delta_{ij} \right) \right] \tag{2}$$

where u_i and f_i are the velocity and body force in the i direction, p is the mixture pressure, μ is the laminar viscosity and μ_t is the turbulent viscosity which is closed by the PANS turbulence model. The mixture density, ρ, is defined as:

$$\rho = \alpha_v \rho_v + (1 - \alpha_v)\rho_1 \tag{3}$$

where α is the volume fraction of one component. The subscripts v and l refer to the vapor and liquid components.

2.1. PANS turbulence model

The modeling challenge in PANS is to determine the closure model as a function of the ratio of the unresolved-to-total kinetic energy, f_k, and the ratio of the unresolved-to-total dissipation, f_e, which are defined as the following:

$$f_k = \frac{k_u}{k}, \quad f_\varepsilon = \frac{\varepsilon_u}{\varepsilon} \tag{4}$$

where k is the total turbulent kinetic energy, ε is the dissipation rate, and the subscript u refers to the unresolved quantities.

The turbulent governing equations in the PANS model from the standard k–ε model are:

$$\frac{\partial (\rho k_u)}{\partial t} + \frac{\partial (\rho u_j k_u)}{\partial x_j} = \frac{\partial}{\partial x_j}\left[(\mu + \frac{\mu_t}{\sigma_{ku}})\frac{\partial k_u}{\partial x_j} \right] + P_{ku} - \rho\varepsilon_u \tag{5}$$

$$\frac{\partial (\rho\varepsilon_u)}{\partial t} + \frac{\partial (\rho u_j\varepsilon_u)}{\partial x_j} = \frac{\partial}{\partial x_j}\left[\left(\mu + \frac{\mu_t}{\sigma_{\varepsilon u}}\right)\frac{\partial \varepsilon_u}{\partial x_j} \right] + C_{\varepsilon1}P_{ku}\frac{\varepsilon_u}{k_u} - C_{\varepsilon2}^*\rho\frac{\varepsilon_u^2}{k_u} \tag{6}$$

where P_{ku} in Eqs. (5) and (6) is the unresolved scale production term. The unresolved kinetic energy, the dissipation Prandtl numbers and $C_{\varepsilon2}^*$ are given by:

$$\sigma_{ku} = \sigma_k\frac{f_k^2}{f_\varepsilon}, \quad \sigma_{\varepsilon u} = \sigma_\varepsilon\frac{f_k^2}{f_\varepsilon} \tag{7}$$

$$C_{\varepsilon2}^* = C_{\varepsilon1} + \frac{f_k}{f_\varepsilon}(C_{\varepsilon2} - C_{\varepsilon1}) \tag{8}$$

where $C_{\varepsilon1}$ = 1.44, $C_{\varepsilon2}$ = 1.92, σ_k = 1.0 and σ_ε = 1.3.

A smaller f_k gives a finer filter. Girimaji (2006) noted that the PANS equations are identical to the RANS equations, but with different model coefficients, which enables the PANS model to be easily implemented into computational fluid dynamics (CFD) codes without any significant changes. Only the model coefficients in Eqs. (7) and (8) need to be modified to implement the PANS turbulence model.

2.2. Cavitation model

The cavitation model is based on the assumption that the water and vapor mixture in the cavitating flow can be modeled as a homogeneous fluid. The cavitation process is governed by the transport equation for the conservation of the vapor (or liquid) volume fraction or the vapor (or liquid) mass fraction with the mass transfer between the liquid and vapor. The source term for the specific interphase mass transfer rate can be modeled by various
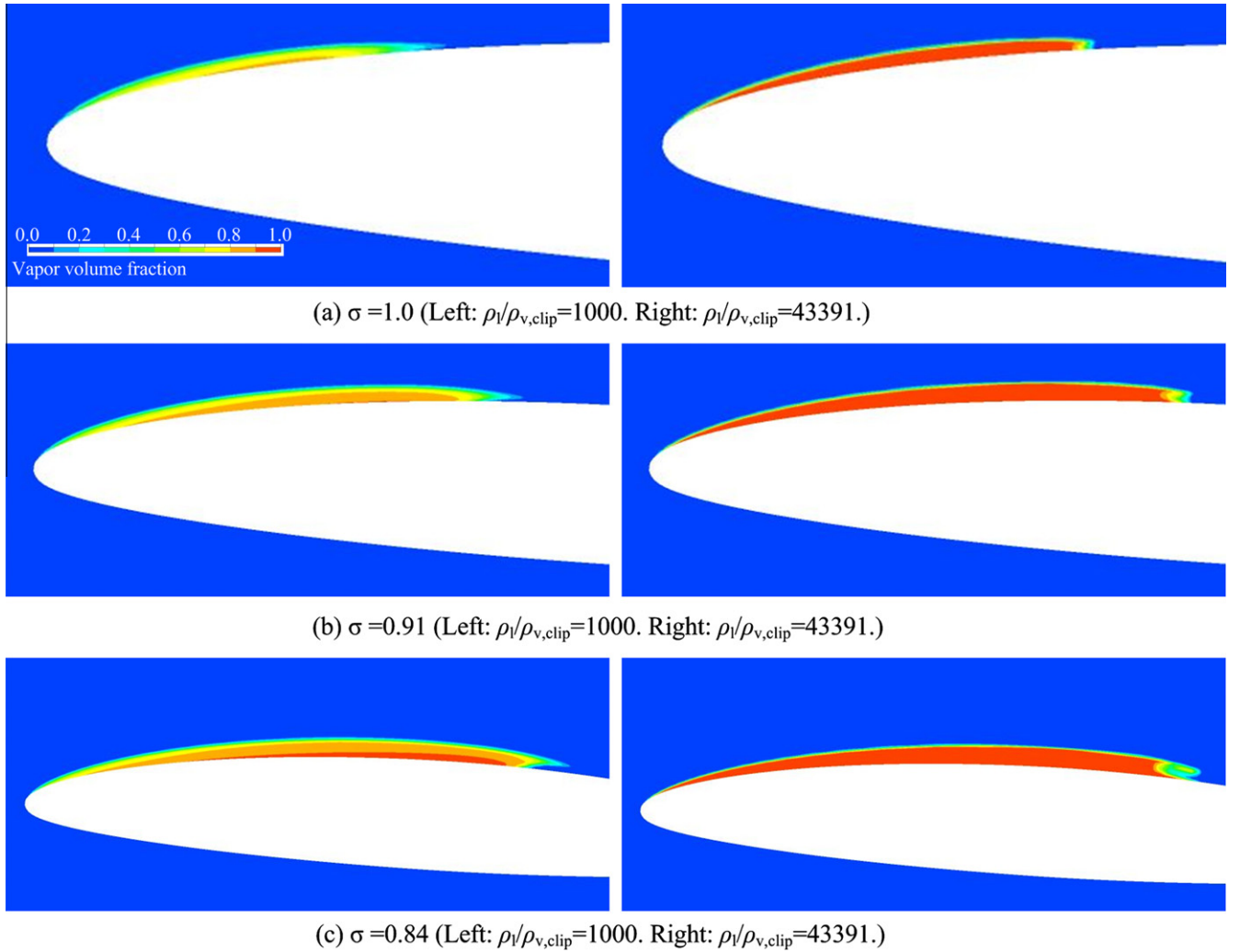
(a) σ =1.0 (Left: $\rho_l/\rho_{v,\text{clip}}$=1000. Right: $\rho_l/\rho_{v,\text{clip}}$=43391.)

(b) σ =0.91 (Left: $\rho_l/\rho_{v,\text{clip}}$=1000. Right: $\rho_l/\rho_{v,\text{clip}}$=43391.)

(c) σ =0.84 (Left: $\rho_l/\rho_{v,\text{clip}}$=1000. Right: $\rho_l/\rho_{v,\text{clip}}$=43391.)

Fig. 1. Calcuated cavity shapes for three cavitation numbers using different maximum density ratios.

cavitation models (Kunz et al., 2000; Schnerr and Sauer, 2001; Senocak and Shyy, 2004a; Singhal et al., 2002; Zwart et al., 2004).

The present paper analysis uses the Zwart model derived from a simplified Rayleigh–Plesset equation which neglects the second-order derivative of the bubble radius (Zwart et al., 2004). During the cavitation simulation in ANSYS-CFX, the vapor density is clipped in a user-controlled fashion by the maximum density ratio, $\rho_l/\rho_{v,\text{clip}}$, to enhance numerical stability. The maximum density ratio is used to clip the vapor density for all terms except the cavitation source term itself, which will use the true density specified as the material property.

In ANSYS-CFX, the vapor volume fraction is governed by the following equation:

$$\frac{\partial(\rho_{v,\text{clip}}\alpha_v)}{\partial t} + \frac{\partial(\rho_{v,\text{clip}}\alpha_v u_j)}{\partial x_j} = \dot{m} \tag{9}$$

$$\dot{m} = C_e \frac{3\rho_v(1-\alpha_v)\alpha_{\text{nuc}}}{R_b}\sqrt{\frac{2}{3}\frac{\max(p_v-p,0)}{\rho_1}} - C_c\frac{3\rho_v\alpha_v}{R_b}$$
$$\times \sqrt{\frac{2}{3}\frac{\max(p-p_v,0)}{\rho_1}} \tag{10}$$

where ρ_l, ρ_v and $\rho_{v,\text{clip}}$ are the liquid density (998 kg/m^3), vapor densities (0.023 kg/m^3), and clipped vapor density which is calculated according to the maximum density ratio. C_e and C_c are empirical coefficients for the vaporization and condensation processes,

α_{nuc} is the non-condensable gas fraction in the liquid, and R_b is the typical bubble size in the water. These empirical constants were set to C_e = 50, C_c = 0.01, α_{nuc} = 5 × 10^{-4} and R_b = 1 × 10^{-6} m based on the work by Zwart et al. (2004), which were validated in various studies (Ji et al., 2012a, 2010, 2011, 2012b; Mejri et al., 2006).

In order to show the effect of maximum density ratio, $\rho_l/\rho_{v,\text{clip}}$, the equation can be rewritten as:

$$\frac{\partial(\rho_v\alpha_v)}{\partial t} + \frac{\partial(\rho_v\alpha_v u_j)}{\partial x_j} = \dot{m}^* \tag{11}$$

$$\dot{m}^* = \frac{\rho_1/\rho_{v,\text{clip}}}{\rho_1/\rho_v}\dot{m} \tag{12}$$

It is noted that the mass transfer source term, $\dot{m}^*$, is proportional to the maximum density ratio, $\rho_l/\rho_{v,\text{clip}}$. According to previous study by present author (Ji, 2011) and other researcher's work (Senocak and Shyy, 2004a), the maximum density ratio between the liquid and the vapor, $\rho_l/\rho_{v,\text{clip}}$, can influence the compressibility characteristics in the cavitation area and the mass transfer between the liquid and vapor. Since this issue is very important, it will be discussed later in the paper.

2.3. Effect of maximum density ratio

The PANS model with f_k = 1.0 (equivalent to the standard k–ε turbulence model) was used to study a stable cavity around a

(a) $\sigma = 1.0$ (Left: $\rho_l/\rho_{v,clip}=1000$. Right: $\rho_l/\rho_{v,clip}=43391$.)

(b) $\sigma = 0.91$ (Left: $\rho_l/\rho_{v,clip}=1000$. Right: $\rho_l/\rho_{v,clip}=43391$.)

(c) $\sigma = 0.84$ (Left: $\rho_l/\rho_{v,clip}=1000$. Right: $\rho_l/\rho_{v,clip}=43391$.)
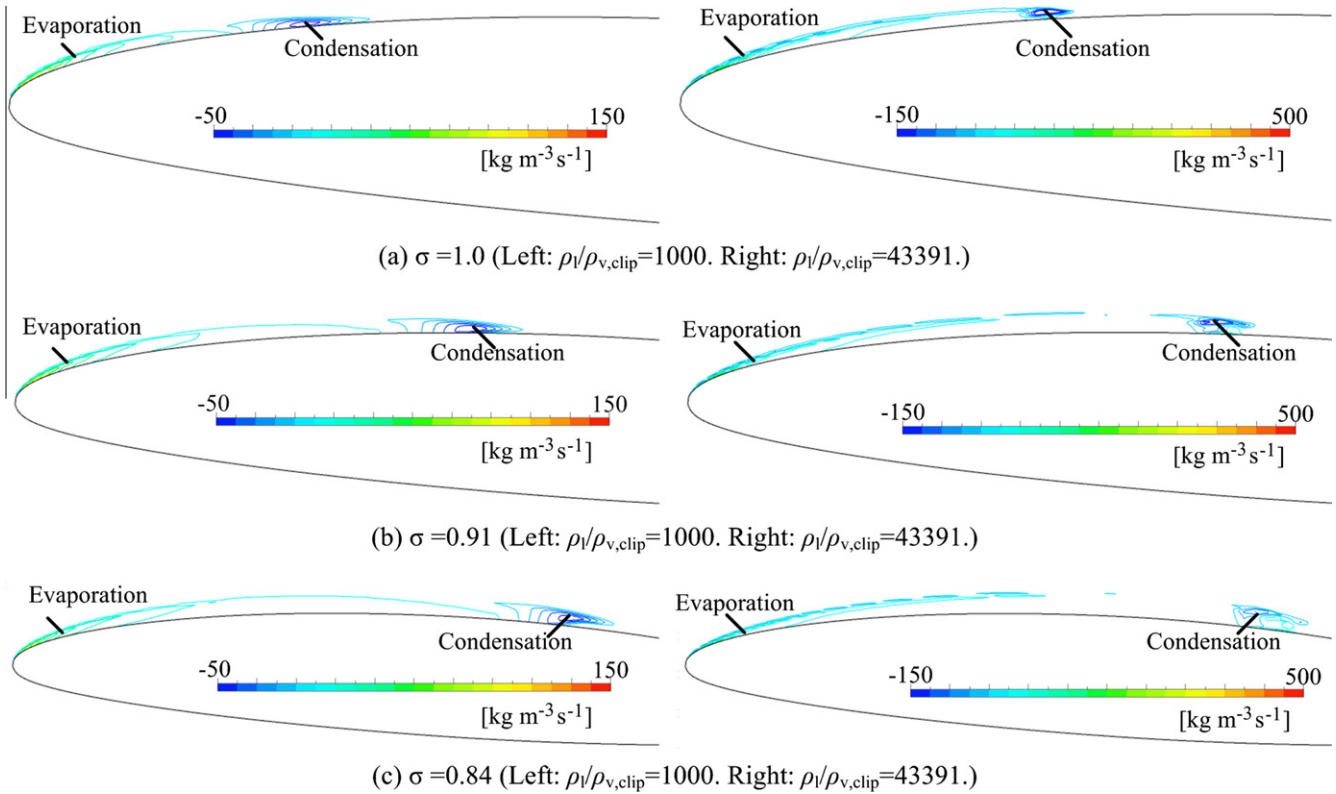
Fig. 2. Contour distribution of mass transfer source term for three cavitation numbers around NACA66(MOD) hydrofoil using different maximum density ratios.
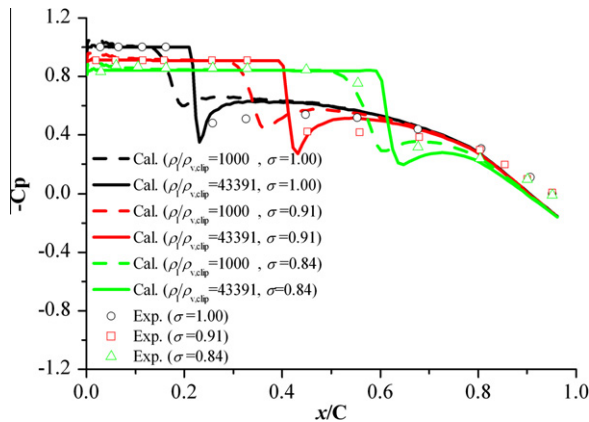

Fig. 3. Comparison of pressure distributions along the suction surface of the hydrofoil.

(a) 3D view

(b) Side view

Fig. 4. Three dimensional twisted hydrofoil.

NACA66(MOD) hydrofoil at a 4° angle of attack, which was experimentally investigated by Shen and Dimotakis (1989). This case has been widely used to validate cavitation models (Ahuja et al., 2001; Morgut et al., 2011; Senocak and Shyy, 2004a). The present simulations were performed for cavitation numbers from 1.0 to 0.84 to investigate the influence of the maximum density ratio. According to the work by Morgut et al. (2011), the default settings of Zwart model might underestimate the mass transfer between liquid and vapor. In present paper, the authors found this poor prediction can be significantly improved by increasing the maximum density ratio from 1000 (ANSYS-CFX default setting) to 43,391 (calculated by $\rho_l = 998$ kg/m^3 and $\rho_v = 0.023$ kg/m^3). The influence of the maximum density ratio for different cavitation numbers is illustrated in Fig. 1. For a constant cavitation number, the cavity length and thickness increase with the maximum
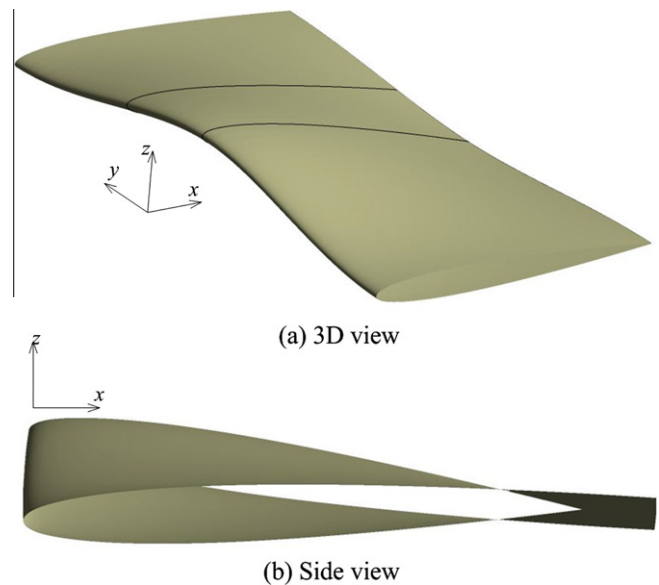
density ratio. Thus, the maximum density ratio may strongly influence the cavity length and pressure distribution along the suction surface of the hydrofoil. The mass transfer from the liquid to the vapor at higher maximum density ratios will produce larger vapor cavity volumes for the same operating conditions. The reason for this is due to the enhanced mass transfer between liquid and vapor, as shown in Fig. 2. Fig. 3 compares the pressure distributions $(-Cp = (p_{ref} - p)/(0.5\rho_l V_\infty^2))$ on the suction surface of the hydrofoil, which shows that the cavity length and pressure distribution
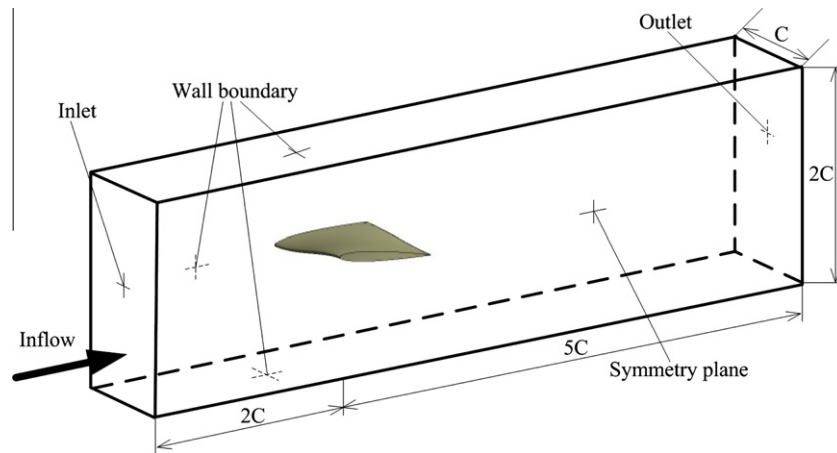
Fig. 5. Computational domain and boundary conditions.

on the wall are well predicted by a maximum density ratio of $\rho_l/\rho_{v,\text{clip}} = 43391$. Lower maximum density ratios (such as $\rho_l/\rho_{v,\text{clip}} = 1000$) accelerate the convergence, but underestimate the cavity development as shown in Fig. 1. Thus, the present mass transfer cavitation model used a maximum density ratio of $\rho_l/\rho_{v,\text{clip}} = 43391$ for simulations of unsteady cavitating flows around a twisted hydrofoil in the following text.

3. Simulation setup

The simulations were conducted by using the CFD code ANSYS-CFX. The PANS turbulence model was input into the code through CEL. The filter control parameters, i.e. the ratio of the unresolved-to-total kinetic energy, f_k, and the ratio of the unresolved-to-total dissipation, f_ε, were specified for the simulations. According to Girimaji (2006), f_ε can be set to unity in high Reynolds number flows such as the present study. The sensitivity study of f_k in the PANS model has been previously reported for unsteady cavitating flows around two-dimensional hydrofoils (Huang and Wang, 2011; Ji, 2011; Ji et al., 2012c), which showed that the cavity shedding structure predicted by the PANS model with $f_k = 0.2$ is consistent with experimental observations due to its better resolution of the kinetic energy and eddy viscosity. Thus, the PANS turbulence model coefficients were set to $f_k = 0.2$ and $f_\varepsilon = 1$ in this study.

The Delft Twist-11 hydrofoil shown in Fig. 4 was analyzed in this research. The hydrofoil is a wing having a rectangular platform of a NACA0009 section with varying attack angles from 0° at the side section to 11° in the mid-section, with symmetry with respect to its mid-span plane. The chord length of the foil is $c = 0.15$ m and the span length is 0.3 m. The attack angle of the entire hydrofoil was −2°.

The computational domain is shown in Fig. 5. The flow simulations used only half of the hydrofoil due to its geometric symmetry. The hydrofoil was located in a channel with height $2c$, a length of $2c$ upstream of the leading edge, a length of $5c$ downstream of the leading edge and a width of c. The inflow velocity was set to $V_\infty = 6.97$ m/s. The static pressure at the outlet plane of the domain, i.e. p_{out}, was assigned according to the cavitation number, $\sigma = (p_{out} - p_v)/(0.5\rho_l V_\infty^2) = 1.07$. The midplane was a symmetry plane. The hydrofoil surface was a non-slip wall while the tunnel walls were used free slip walls. An O–H type grid was generated for the domain with sufficient refinement ($30 \leqslant y^+ \leqslant 100$) towards the foil surface. To better resolve the 3D cavity structure, the mesh along the spanwise direction was carefully checked in non-cavitation condition with three node number, 40, 100 and 150, as shown in Fig. 6. The investigation was performed by monitoring the

minimum and maximum pressures around hydrofoil surface and the values of the lift C_L and drag C_D coefficients, defined as following:

$$C_L = \frac{\text{Lift}}{0.5\rho \times V_\infty^2 \times C \times \text{Span}} \quad C_D = \frac{\text{Drag}}{0.5\rho \times V_\infty^2 \times C \times \text{Span}} \quad (13)$$

From the results shown in Table 1, it is indicated that the differences can be neglected between the medium and fine resolution meshes. Thus, the medium resolution mesh with about 3 million nodes was selected as the final grid.

The time-dependent governing equations were discretized in both space and time. The pressure–velocity direct coupling method (Vanka, 1986) was used to solve the equations. During the unsteady cavitation calculation, convergence evaluation in each physical time step is an important issue during unsteady cavitation simulation. According to the work by Li (2012) and our previous research (Ji, 2011; Ji et al., 2012c), excessive iteration in each time step will cost too much computational resource, while an insufficient iteration can lead to insufficient accuracy. In order to keep balance between computational accuracy and efficiency in present paper, the authors finally selected 20 iterations in each time step and found not only the RMS residuals drop to 10^{-4} but also cavity volume integral becomes almost constant.

The high order resolution scheme (Barth and Jesperson, 1989) was used for the convection terms with the central difference scheme used for the diffusion terms in the governing equations. It should be noted that the high order resolution scheme is a second-order scheme, which can locally switch to first order scheme to prevent numerical oscillations near critical high density gradient areas. So this scheme is both accurate and robust since it only reduces to the first order near discontinuities. The unsteady second-order implicit formulation was used for the transient term. The unsteady cavitating flow simulations were started from a steady non-cavitating flow result. Then the cavitation model and unsteady solver were turned on for the cavitating flow simulation. In order to resolve the real transient evolution of cavitating flow, the time step was set as $\Delta t = 1.076 \times 10^{-4}$ s, which is equivalent to $T_{ref}/200$ ($T_{ref} = c/V_\infty$ where V_∞ is the undisturbed velocity at the domain inlet), as suggested by Coutier-Delgosha et al. (2003).
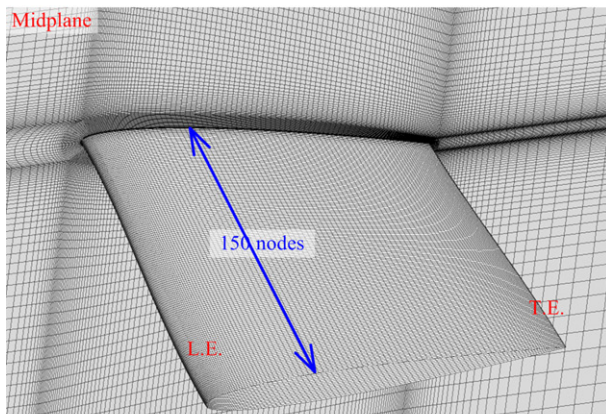
4. Results and discussion

The twisted design and the larger attack angle in the middle area cause the cavitation to mainly develop near the mid-span area close to the leading edge with a curved closure line. As a result, the re-entrant jet is no longer purely a reversed flow going upstream
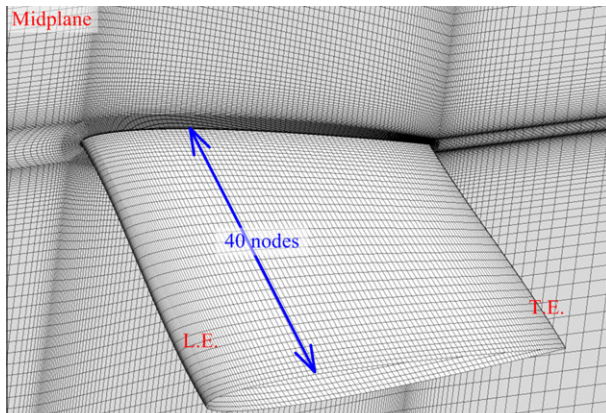
(a) Mesh case 1 (total 1184960 nodes)
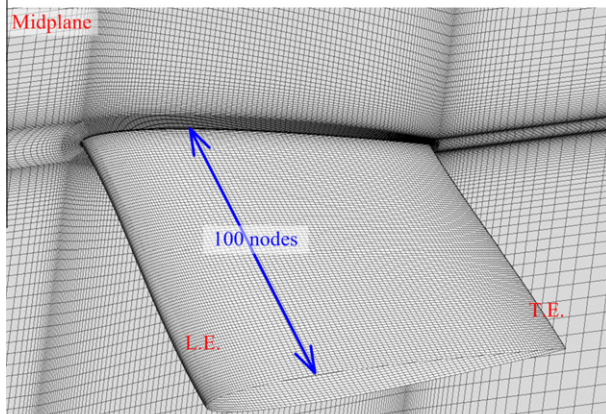
(b) Mesh case 2 (total 2962400 nodes)

(c) Mesh case 3 (total 4443600 nodes)

Fig. 6. Three cases of mesh around the Delft twisted hydrofoil surface.

Table 1
Results of the mesh independence study for twisted hydrofoil.

Mesh	Nodes	p_{min}	p_{max}	C_L	C_D
Case 1 (Coarse)	1,184,960	−52033.3	54246.4	0.4295	0.01454
Case 2 (Medium)	2,962,400	−51970.2	54264.1	0.4296	0.01453
Case 3 (Fine)	4,443,600	−51976.1	54264.7	0.4296	0.01453

but also has a transverse component in the spanwise direction. The combined effect of these two components causes a very complex shedding process.

The evolution of the cavitating flow can be illustrated through the time history of the total vapor volume, V_{cav}, where V_{cav} was defined as:
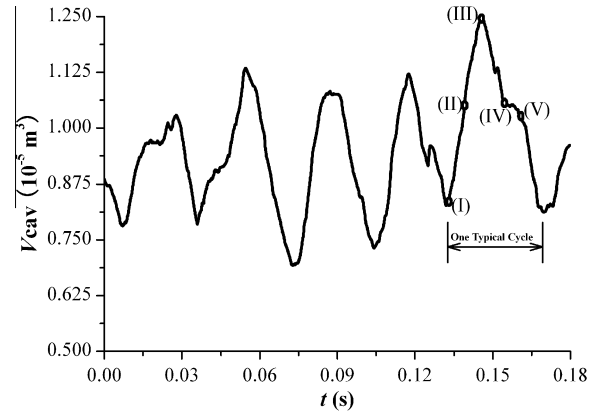

Fig. 7. Variation of the cavity volume.

$$V_{cav} = \sum_{i=1}^{N} \alpha_i V_i \qquad (14)$$

where N is the total number of control volumes in the computational domain, α_i is the vapor volume fraction in each control volume and V_i is the volume of each cell.

The total vapor volume, V_{cav}, is a convenient parameter for understanding the transient behavior of cavitating flows. The total vapor volume calculated at each time step is shown in Fig. 7 with snapshots of five typical instants of cavitating flows with iso-surface values of $\alpha_v = 0.1$ shown in Fig. 8. Fig. 7 indicates that the vapor volume variation due to the cavity shedding from the twisted hydrofoil is periodic. The predicted shedding frequency was about 30.7 Hz, which agrees fairly well with the measured frequency (32.2 Hz (Foeth, 2008)). For comparison, the experimental top view pictures taken by Foeth (2008) are shown at each instant in Fig. 8. The positions of the leading and trailing edges of the hydrofoil as well as the flow direction are marked in these pictures. The predictions agree reasonably well with the experimental observations. A bird's-eye view of the numerical results is displayed on the right to illustrate the evolution of the three-dimensional cavitation patterns.

In Fig. 8a, the total vapor volume is a minimum at instant (I) in Fig. 7 after the attached cavity in the center of the hydrofoil has shed from the leading edge due to the collision between the re-entrant flow and the cavity interface. The shedding cavity then quickly changes from a smooth pocket of vapor into a highly turbulent vapor cloud. This process is the primary shedding event. Then the shedding vapor cloud becomes more turbulent and is advected downstream by the main flow, as shown in Fig. 8b and c. Meanwhile, the tail of the attached cavity begins to curl into a concave shape and grows quickly from the leading edge, which explains the increase in the total vapor volume from instant (I) to instant (III) in Fig. 7. After that the attached cavity grows slowly and the shedding vapor cloud quickly shrinks (Fig. 8d) and finally collapses (Fig. 8e and a), which caused the decrease of total vapor volume in Fig. 7. It should be noted that there is a secondary shedding of both downstream lobes of the remaining attached cavity in Fig. 8d after the primary shedding occurs from the center part of the twisted hydrofoil. It is noted that the primary shedding vapor cloud becomes the horse-shoe vortex structure with a U shape having one head and two legs, with the secondary shedding vapor clouds having the same structures, as shown by the bird's-eye view in Fig. 8d. Fig. 9 shows the flow field in terms of the velocity vectors near the suction surface of the hydrofoil at instant (IV) with clearly defined a radially-diverging re-entrant jet and a pair of side-entrant jets. Foeth (2008) assumed from the experimental observations that the secondary shedding was caused by the collision of
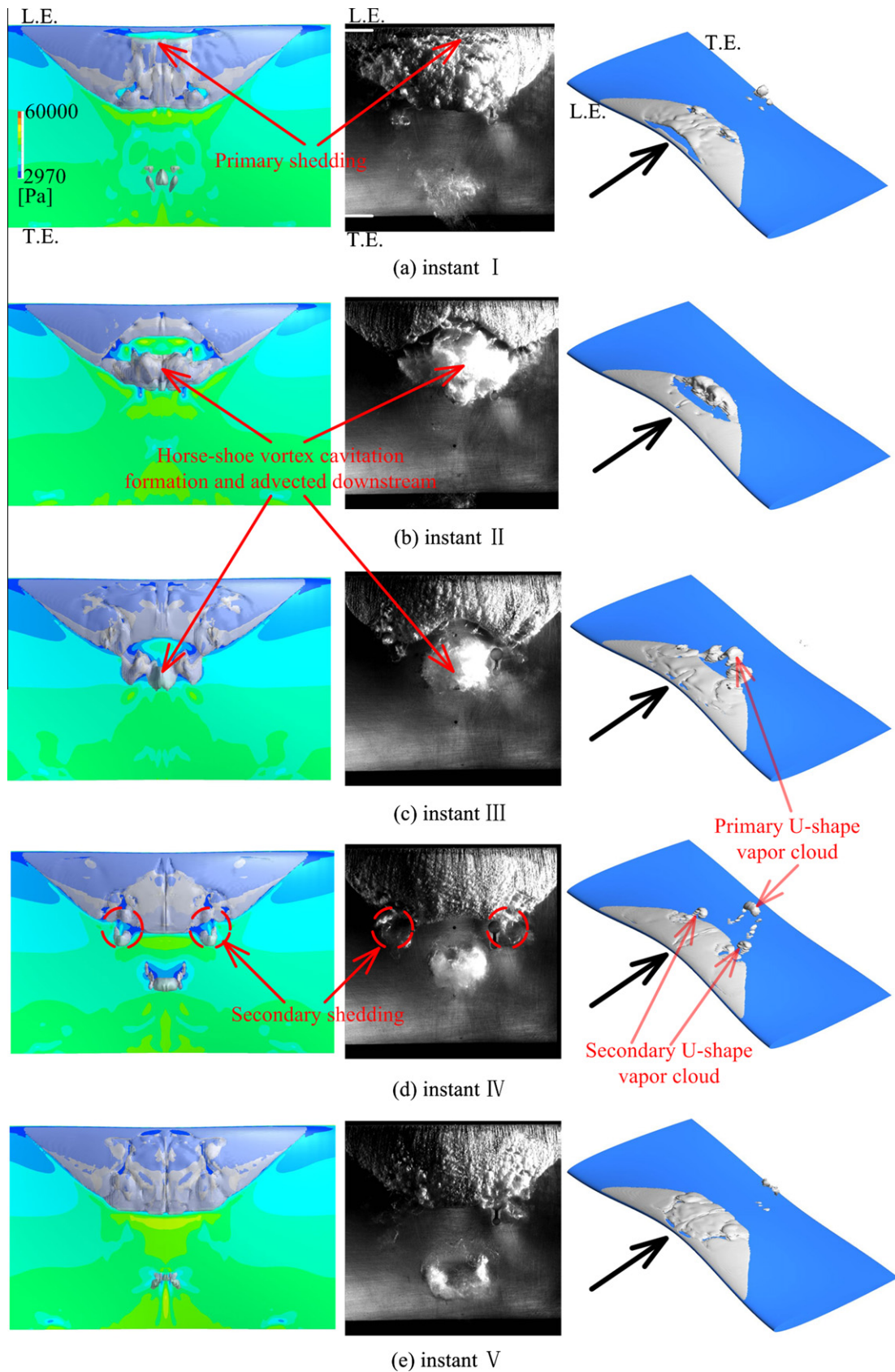
Fig. 8. Cavitation patterns during one cavity shedding cycle (Left: Numerical top view, Middle: Experimental top view, Right: Numerical bird's-eye view.).

the side-entrant jets and the radially-diverging re-entrant jet. These complicated cavitation processes must be attributed to the

three-dimensional effect of the twisted hydrofoil. The re-entrant jet in Fig. 9 then moves further upstream while the attached cavity
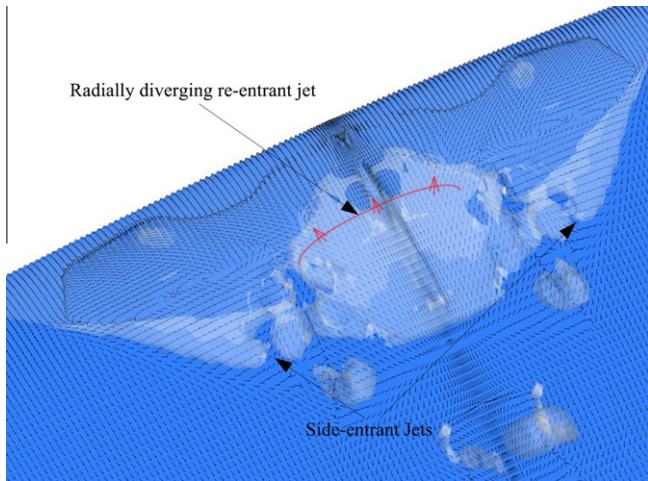
Fig. 9. Re-entrant jet and side-entrant jet development at the instant IV.

length is almost constant and the tail becomes convex and stable as seen in Fig. 8e, even though a local small disturbance was observed along the side of the attached cavity tail in the experiments. Eventually the attached cavity was cut off near the leading edge of the hydrofoil due to the interaction between the re-entrant jet and the attached cavity surface. The total vapor volume decreased to

the minimum value in Fig. 7 until a new cycle started again as seen in Fig. 8a.

Thus, the present simulation reasonably reproduces the cavitation patterns and their evolution around the twisted hydrofoil with primary and secondary shedding vapor clouds. The distinct side-lobes shape of the attached cavity and the formation of radially-diverging re-entrant and side-entrant jets seen in the experimental observations (Foeth, 2008) are well captured by the PANS method.

According to the experimental work by Foeth (2008), a very distinct feature of the shedding vapor cloud around the twisted hydrofoil is the formation of a cavitating horse-shoe vortex structure on the center part of the hydrofoil. Though the three-dimensional attached cavity with the main lobe and the side-lobes shape and the shedding characteristics of the cavitating horse-shoe vortex are well predicted as shown in Fig. 8, the collapse of the shedding vapor cloud is somewhat underestimated in Fig. 8e and a. This tendency is consistent with the simulations using the improved SST k–ω turbulence model (Li et al., 2010) and LES simulations (Bensow, 2011). Kubota et al. (1989) observed that the vapor clouds had a concentrated vorticity region at their center and contained clusters of many small cavitation bubbles, which would be beyond the ability of present CFD cavitating simulations based on the homogeneous flow treatment.

In order to illustrate the evolution of shedding horse-shoe vortex structure effectively, the side view of the cavity shedding is shown by plotting of the vapor fraction iso-surfaces with $\alpha_v = 0.1$ as shown on the left in Fig. 10. In the right picture of
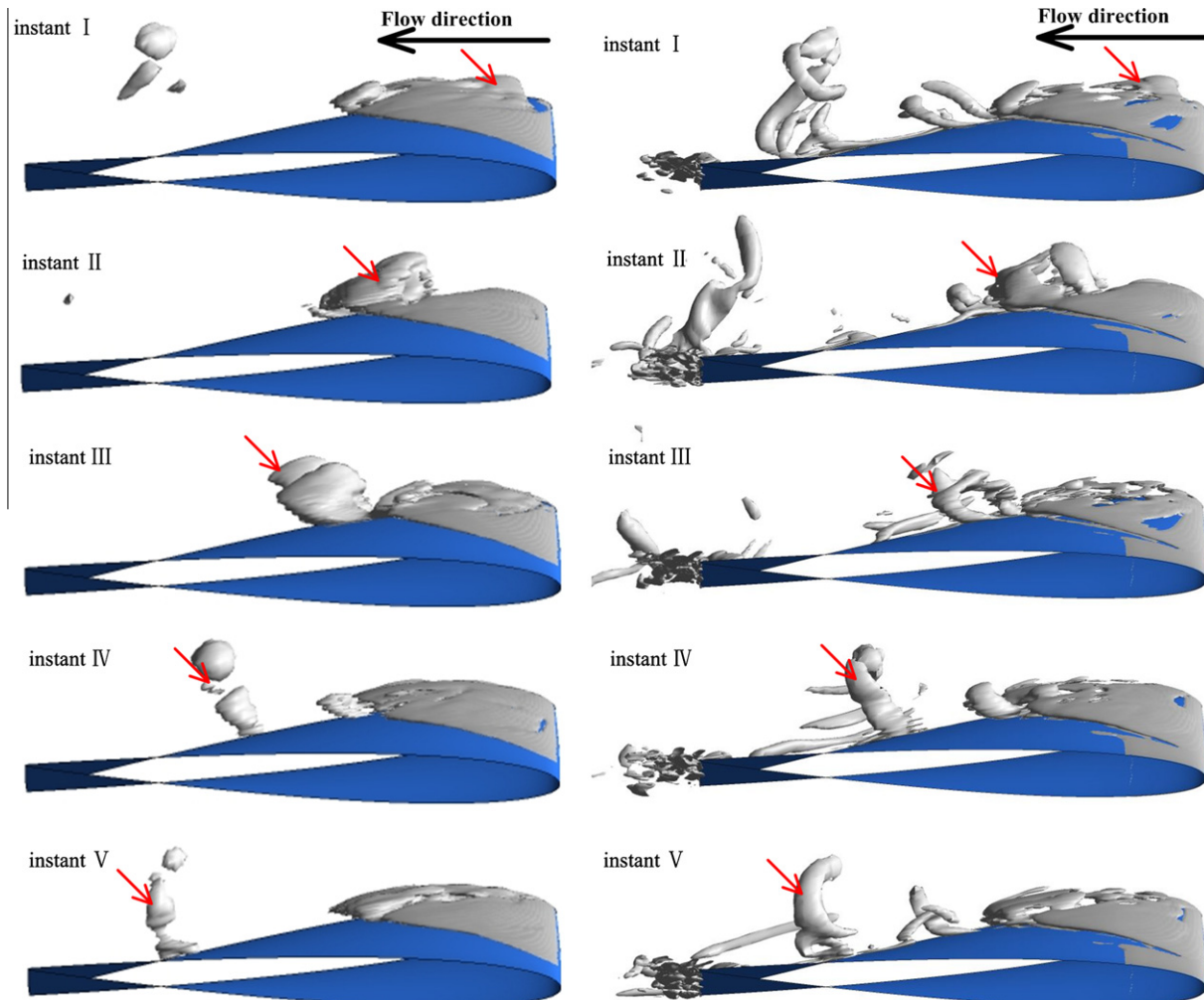

Fig. 10. Side views of the horse-shoe vortex during a cavity shedding cycle (Left: iso-surface $\alpha_v = 0.1$, Right: dimensionless Q iso-surface = 200.).
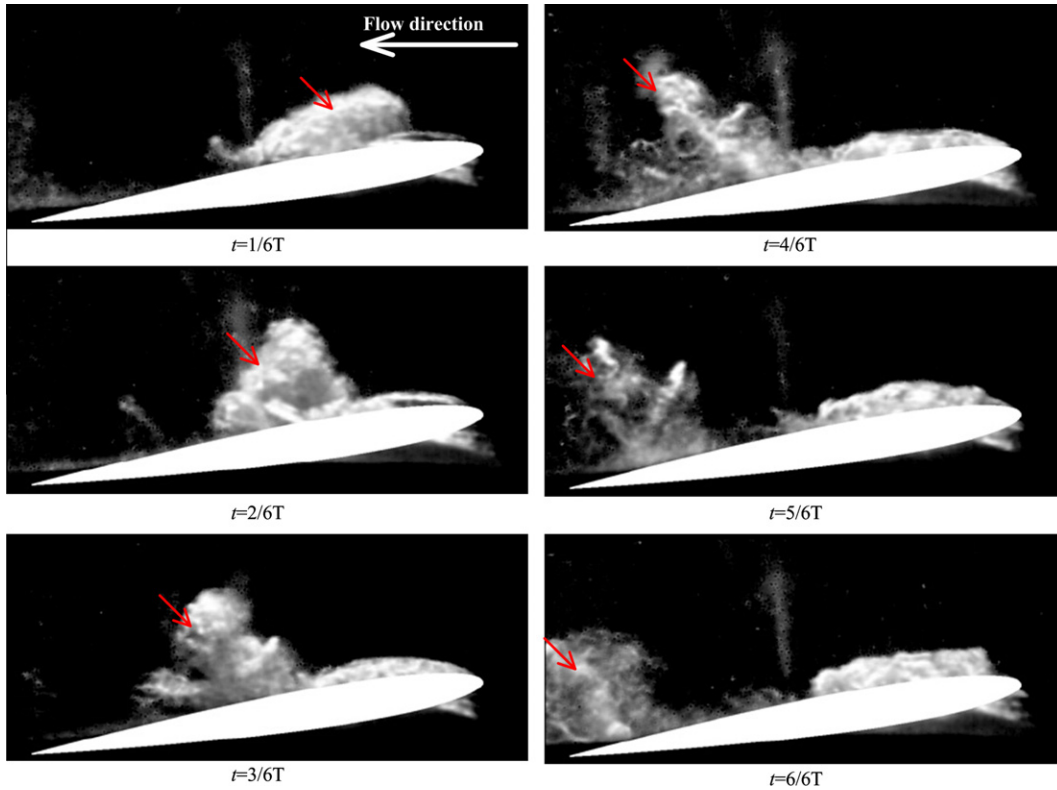
Fig. 11. Side view of the horse-shoe vortex by PIV images analysis (Foeth, 2008).
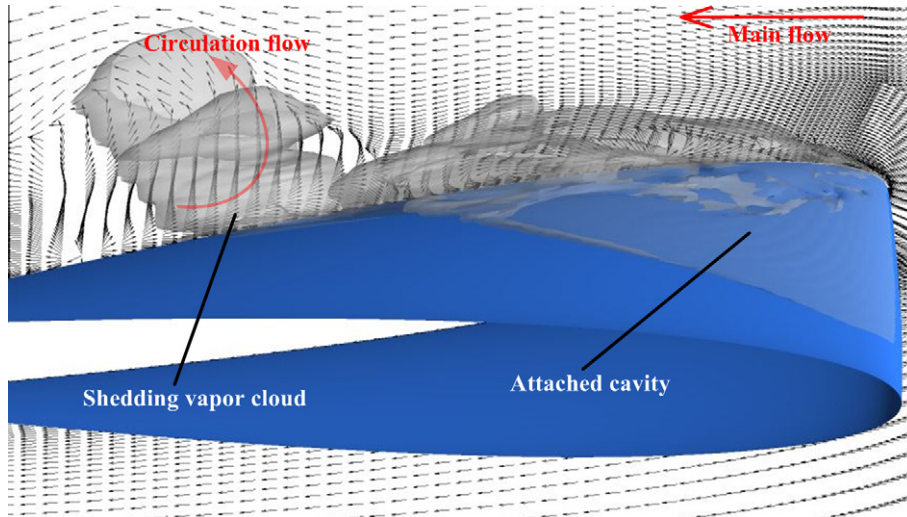

Fig. 12. Velocity field at instant (III).

Fig. 10, the flow structures are visualized based on the Q-criterion to identify the vortices. Positive non-dimensional values of the Q-criterion, defined as the second invariant of the velocity gradient tensor (Hunt et al., 1988), are given by,

$$Q = \frac{1}{2}\left(\frac{c}{V_\infty}\right)^2\left[\left(\frac{\partial u_i}{\partial x_t}\right)^2 - \frac{\partial u_i}{\partial x_j}\frac{\partial u_j}{\partial x_i}\right] \qquad (15)$$

For the present case, the iso-surface of the Q-criterion was set 200 to visualize the turbulent cavitating flow. The experimental visualizations of the cavity interface using PIV image analysis from the side view (Foeth, 2008; Foeth et al., 2006) are shown in Fig. 11.

From Figs. 10 and 11 (side view) as well as Fig. 8 (top view and bird's-eye view), we can clearly observe the cavity shedding process and the formation and convection of a cavitating horse-shoe vortex. The transport of the shedding horse-shoe structure towards the trailing edge is governed by the main flow around the hydrofoil. The center of the shedding structure is raised above the hydrofoil by the flow circulation due to the largest attack angle in the midplane, e.g. at instant (III) as shown in Fig. 12, with this process being closely related to the vortex movement. These results suggest that the interaction between the circulating flow and the shedding vapor cloud is closely related to the formation of the horse-shoe vortex.

The height of the horse-shoe vortex indicated by the arrow in Fig. 10 increases as seen from the side view as it moves downstream, which is also consistent with the experimental
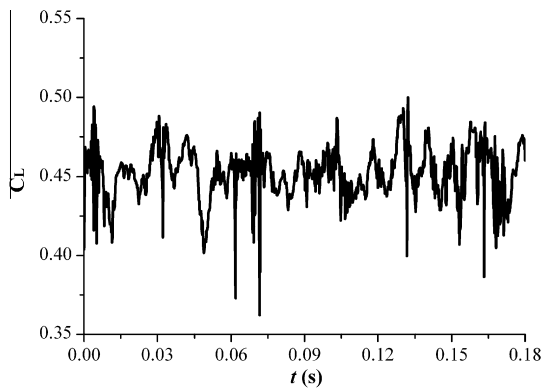
Fig. 13. Time-dependent lift coefficient over several cycles.

Table 2
Time-averaged lift coefficients predicted by various model.

	Cal.	Exp.	Error (%)
RANS SST k–ω with correction (Li et al., 2010)	0.43	0.5167	17
RANS SA with correction (Bensow, 2011)	0.43		17
Implicit LES (Bensow, 2011)	0.45		13
PANS by present	0.453		12

observations by Gopalan and Katz (2000). According to Gopalan and Katz, the flow downstream of the closure region contains hairpin-like structures containing bubbles. In Fig. 10, the predicted horse-shoe vortex given by the non-dimensional Q-criterion iso-surface is more complicated than what we can see from iso-surface value of vapor fraction and agrees well with the experiments shown in Fig. 11. It should be noted that the volume of the horse-shoe vortex given by iso-surface of 10% vapor volume fraction is slightly underestimated, perhaps due to the compressibility and bubble cloud effects not included in the present calculation. The experiments (Foeth, 2008) indicated that the shedding vapor is bubble clusters, which will influence the fluid compressibility and wave speed, and affect the collapsing behavior.

Once the cavity shedding occurs, the lift force on the hydrofoil must vary dramatically as the pressure distribution changes. Fig. 13 shows the time-dependent numerical prediction for the lift coefficient, C_L, which is calculated at each time step.

The evolution of the lift coefficient during the cavity shedding is very complicated with the PANS model resolving more of the turbulent kinetic energy and overcoming the RANS over-predictions of the turbulent viscosity at the rear part of the cavity (Huang and Wang, 2011). The time averaged lift coefficient is 0.453, which is 12% lower than the experimentally measured value of 0.5167 (Foeth, 2008). This prediction of the time averaged lift coefficient is much more accurate than the RANS result of Li et al.(2010) and is equivalent to that of the LES results of Bensow (2011) as shown in Table 2. This may be attributed to better resolution of the turbulent cavitating flow around the hydrofoil surface by the PANS method.

5. Conclusions

Unsteady cavitating turbulent flow around hydrofoils was simulated using the Partially-Averaged Navier–Stokes method and a mass transfer cavitation model with consideration of the maximum density ratio effect. Based on the numerical results, several conclusions can be drawn as follows:

(1) The cavity length and thickness as well as the pressure distribution along suction surface of the hydrofoil can be satisfactorily predicted for stable cavities by using the proposed numerical method.

(2) The unsteady cavitation patterns and their evolution around the Delft twisted hydrofoil with dramatic cavity volume fluctuations are captured by the present method. The predicted three-dimensional cavity structures vary along the span due to the variation of attack angle in the spanwise direction, with cavity growth, destabilization, and collapse. The shedding cycle as well as its frequency agrees fairly well with experimental observations. The simulations show that the distinct side-lobes shape of the attached cavity and the U-shaped shedding cavitating horse-shoe vortex during cavitation development. Furthermore, it is shown that the shedding cavitating horse-shoe vortex includes a primary U-shape vapor cloud and two secondary U-shape vapor clouds originating from the primary shedding at the cavity center and the secondary shedding at both cavity sides. The primary shedding is related to the collision of the radially-diverging re-entrant jet and the attached cavity surface, while the secondary shedding is due to the collision of the side-entrant jets and the radially-diverging re-entrant jet. The local flow fields demonstrate that the interaction between the circulating flow and the shedding vapor cloud is the main mechanism for the cavitating horse-shoe vortex production.

(3) Two series of side views by 10% vapor volume fraction iso-surfaces and the non-dimensional Q-criterion of 200 are used to illustrate the evolution of the horse-shoe vortex, i.e. the formation, roll-up and transport. It is shown that the height of the shedding horse-shoe vortex increases as it moves downstream, with the vortex shape given by the non-dimensional Q-criterion being more complicated than that of the vapor fraction iso-surface which is consistent with the experimental observations.

(4) The results also show that the accuracy of the time-averaged lift coefficient predicted by PANS calculation is better than that predicted by other methods based on RANS solvers, though the computed lift is about 12% lower than the measured value.

(5) Thus, the PANS method can be used to reproduce the complicated cavitation phenomena and the mechanism for the interaction between the cavitation and turbulence. Therefore, this can be used to provide substantial fundamental information for improving cavitating flow simulations.

References

Ahuja, V., Hosangadi, A., Arunajatesan, S., 2001. Simulations of cavitating flows using hybrid unstructured meshes. J. Fluids Eng.-Trans. ASME 123, 331–340.
Arndt, R.E.A., 1981. Cavitation in fluid machinery and hydraulic structures. Annu. Rev. Fluid Mech. 13, 273–328.
Barth, T.J., Jesperson, D.C., 1989. The design and application of upwind schemes on unstructured meshes. In: Proceedings of the 27th Aerospace Sciences Meeting, Reno, Nevada.

Bensow, R.E., 2011. Simulation of the unsteady cavitation on the the Delft Twist11 foil using RANS, DES and LES. In: Proceedings of the 2nd International Symposium on Marine Propulsors, Hamburg, Germany.

Coutier-Delgosha, O., Reboud, J.L., Delannoy, Y., 2003. Numerical simulation of the unsteady behaviour of cavitating flows. Int. J. Numer. Methods Fluids 42, 527–548.

Dang, J., Kuiper, G., 1999. Re-entrant jet modeling of partial cavity flow on two-dimensional hydrofoils. J. Fluids Eng.-Trans. ASME 121, 773–780.

De Lange, D.F., De Bruin, G.J., 1998. Sheet cavitation and cloud cavitation, re-entrant jet and three-dimensionality. Appl. Sci. Res. 58, 91–114.

Dular, M., Bachert, R., Schaad, C., Stoffel, B., 2007. Investigation of a re-entrant jet reflection at an inclined cavity closure line. Eur. J. Mech. B-Fluid 26, 688–705.

Foeth, E.J., 2008. The Structure of Three-Dimensional Sheet Cavitation, Mechanical Maritime and Materials Engineering, Ph.D. Thesis, Delft University of Technology, Wageningen, the Netherlands.

Foeth, E.J., van Doorne, C.W.H., van Terwisga, T., Wieneke, B., 2006. Time Resolved PIV and Flow Visualization of 3D Sheet Cavitation. Exp. Fluids 40, 503–513.

Foeth, E.J., van Terwisga, T., van Doorne, C., 2008. On the collapse structure of an attached cavity on a three-dimensional hydrofoil. J. Fluids Eng.-Trans. ASME 130, 071303.

Girimaji, S.S., 2006. Partially-Averaged Navier-Stokes Model for Turbulence. A Reynolds-Averaged Navier-Stokes to Direct Numerical Simulation Bridging Method. J Appl Mech-Trans. ASME 73, 413–421.

Goncalves, E., 2011. Numerical Study of Unsteady Turbulent Cavitating Flows. Eur. J. Mech. B-Fluid 30, 26–40.

Gopalan, S., Katz, J., 2000. Flow structure and modeling issues in the closure region of attached cavitation. Phys. Fluids 12, 895–911.

Hoekstra, M., van Terwisga, T., Foeth, E.J., 2011. smp'11 Workshop – Case 1: DelftFoil. In: Proceedings of the 2nd International Symposium on Marine Propulsors, Hamburg, Germany.

Huang, B.A., Wang, G.Y., 2011. Partially averaged Navier-Stokes method for time-dependent turbulent cavitating flows. J. Hydrodyn. 23, 26–33.

Hunt, J.C.R., Wray, A.A., Moin, P., 1988. Eddies, streams, and convergence zones in turbulent flows. In: Proceedings of the 1988 Summer Program In its Studying Turbulence Using Numerical Simulation Databases, 2. (SEE N89–24538 18–34), Center for Turbulence Research.

Jeong, E., Girimaji, S.S., 2010. Partially averaged Navier-Stokes (PANS) method for turbulence simulations-flow past a square cylinder. J. Fluids Eng.-Trans. ASME 132, 121203.

Ji, B., 2011. Study on Cavitating Flow and Its Induced Pressure Fluctuations around Marine Propeller in Non-Uniform Wake. Ph.D. Thesis, Tsinghua University, Beijing, China.

Ji, B., Luo, X.W., Peng, X.X., Wu, Y.L., Xu, H.Y., 2012a. Numerical analysis of cavitation evolution and excited pressure fluctuation around a propeller in non-uniform wake. Int. J. Multiphas. Flow 43, 13–21.

Ji, B., Luo, X.W., Peng, X.X., Zhang, Y., Wu, Y.L., Xu, H.Y., 2010. Numerical investigation of the ventilated cavitating flow around an under-water vehicle based on a three-component cavitation model. J. Hydrodyn. 22, 753–759.

Ji, B., Luo, X.W., Wang, X., Peng, X.X., Wu, Y.L., Xu, H.Y., 2011. Unsteady numerical simulation of cavitating turbulent flow around a highly skewed model marine propeller. J. Fluids Eng.-Trans. ASME 133, 011102.

Ji, B., Luo, X.W., Wu, Y.L., Peng, X.X., Xu, H.Y., 2012b. Partially-Averaged Navier–Stokes method with modified k–ε model for cavitating flow around a marine propeller in a non-uniform wake. Int J Heat Mass Tran 55, 6582–6588.

Ji, B., Luo, X.W., Wu, Y.L., Xu, H.Y., 2012c. Unsteady cavitating flow around a hydrofoil simulated using partially-averaged navier-stokes model. Chin. Phys. Lett. 29, 076401.

Kawanami, Y., Kato, H., Yamaguchi, H., Maeda, M., Nakasumi, S., 2002. Inner structure of cloud cavity on a foil section. JSME Int. J. B-Fluid Thermal 45, 655–661.

Kawanami, Y., Kato, H., Yamaguchi, H., Tanimura, M., Tagaya, Y., 1997. Mechanism and control of cloud cavitation. J. Fluids Eng.-Trans. ASME 119, 788–794.

Kjeldsen, M., Arndt, R.E.A., Effertz, M., 2000. Spectral characteristics of sheet/cloud cavitation. J. Fluids Eng.-Trans. ASME 122, 481–487.

Koop, A.H., Hoeijmakers, H.W.M., 2009. Numerical simulation of unsteady three-dimensional sheet cavitation. In: Proceedings of the 7th International Symposium on Cavitation, Michigan, USA.

Kubota, A., Kato, H., Yamaguchi, H., Maeda, M., 1989. Unsteady structure measurement of cloud cavitation on a foil section using conditional sampling technique. J. Fluids Eng.-Trans. ASME 111, 204–210.

Kunz, R.F., Boger, D.A., Stinebring, D.R., Chyczewski, T.S., Lindau, J.W., Gibeling, H.J., Venkateswaran, S., Govindan, T.R., 2000. A preconditioned Navier-Stokes method for two-phase flows with application to cavitation prediction. Comput. Fluids 29, 849–875.

Laberteaux, K.R., Ceccio, S.L., 2001a. Partial cavity flows. Part 1. Cavities forming on models without spanwise variation. J. Fluid Mech. 431, 1–41.

Laberteaux, K.R., Ceccio, S.L., 2001b. Partial cavity flows. Part 2. Cavities forming on test objects with spanwise variation. J. Fluid Mech. 431, 43–63.

Lakshmipathy, S., Girimaji, S.S., 2007. Extension of Boussinesq turbulence constitutive relation for bridging methods. J. Turbul. 8, 1–21.

Lakshmipathy, S., Girimaji, S.S., 2010. Partially averaged Navier-Stokes (PANS) method for turbulence simulations: flow past a circular cylinder. J. Fluids Eng.-Trans. ASME 132, 121202.

Le, Q., Franc, J.P., Michel, J.M., 1993. Partial cavities – global behavior and mean pressure distribution. J. Fluids Eng.-Trans. ASME 115, 243–248.

Li, D.Q., Grekula, M., Lindell, P., 2010. Towards numerical prediction of unsteady sheet cavitation on hydrofoils. J. Hydrodyn. 22, 741–746.

Li, Z.R., 2012. Assessment of Cavitation Erosion with a Multiphase Reynolds-Averaged Navier-Stokes Method. Ph.D. Thesis, Delft University of Technology, Wageningen, the Netherlands.

Ma, J.M., Peng, S.H., Davidson, L., Wang, F.J., 2011. A low Reynolds number variant of partially-averaged Navier-Stokes model for turbulence. Int. J. Heat Fluid Flow 32, 652–669.

Mejri, I., Bakir, F., Rey, R., Belamri, T., 2006. Comparison of computational results obtained from a homogeneous cavitation model with experimental investigations of three inducers. J. Fluids Eng.-Trans. ASME 128, 1308–1323.

Morgut, M., Nobile, E., Bilus, I., 2011. Comparison of mass transfer models for the numerical prediction of sheet cavitation around a hydrofoil. Int. J. Multiphase Flow 37, 620–626.

Pham, T.M., Larrarte, F., Fruman, D.H., 1999. Investigation of unsteady sheet cavitation and cloud cavitation mechanisms. J. Fluids Eng.-Trans. ASME 121, 289–296.

Reisman, G.E., Wang, Y.C., Brennen, C.E., 1998. Observations of shock waves in cloud cavitation. J. Fluid Mech. 355, 255–283.

Saito, Y., Takami, R., Nakamori, I., Ikohagi, T., 2007. Numerical analysis of unsteady behavior of cloud cavitation around a NACA0015 Foil. Comput. Mech. 40, 85–96.

Salvatore, F., Streckwall, H., van Terwisga, T., 2009. Propeller cavitation modelling by CFD results from VIRTUE 2008 Rome workshop. In: Proceedings of the 1st International Symposium on Marine Propulsors, Trondheim, Norway.

Schnerr, G.H., Sauer, J., 2001. Physical and numerical modeling of unsteady cavitation dynamics. In: Proceedings of 4th International Conference on Multiphase Flow, New Orleans, USA.

Schnerr, G.H., Sezal, I.H., Schmidt, S.J., 2008. Numerical investigation of three-dimensional cloud cavitation with special emphasis on collapse induced shock dynamics. Phys. Fluids 20, 040703.

Senocak, I., Shyy, W., 2004a. Interfacial dynamics-based modelling of turbulent cavitating flows, Part-1: Model development and steady-state computations. Int. J. Numer. Methods Fluids 44, 975–995.

Senocak, I., Shyy, W., 2004b. Interfacial Dynamics-based modelling of turbulent cavitating flows, Part-2: Time-dependent computations. Int. J. Numer. Methods Fluids 44, 997–1016.

Shen, Y.T., Dimotakis, P.E., 1989. The influence of surface cavitation on hydrofynamic forces. In: Proceedings of the 22nd American Towing Tank Conference, Newfoundland, Canada.

Singhal, A.K., Athavale, M.M., Li, H.Y., Jiang, Y., 2002. Mathematical basis and validation of the full cavitation model. J. Fluids Eng.-Trans. ASME 124, 617–624.

Song, C.S., Park, S.O., 2009. Numerical simulation of flow past a square cylinder using partially-averaged Navier-Stokes model. J. Wind Eng. Ind. Aerod. 97, 37–47.

Stutz, B., Reboud, J.L., 1997. Experiments on unsteady cavitation. Exp. Fluids 22, 191–198.

Vanka, S.P., 1986. Block-implicit multigrid solution of Navier-Stokes equations in primitive variables. J. Comput. Phys. 65, 138–158.

Zwart, P.J., Gerber, A.G., Belamri, T., 2004. A two-phase flow model for predicting cavitation dynamics. In: Proceedings of International Conference on Multiphase Flow, Yokohama, Japan.